

# Melt pool signatures of TiN nanoparticle dry-coated $\text{Co}_{25}\text{Cr}_{25}\text{Fe}_{25}\text{Ni}_{25}$ metal powder in laser-powder-bed-fusion

Eric Gärtner <sup>a,b</sup>, Arne Witte <sup>a,b</sup>, Nicolas J. Peter <sup>c</sup>, Vivek Devulapalli <sup>c</sup>, Nils Ellendt <sup>a,b</sup>, Gerhard Dehm <sup>c</sup>, Eric A. Jägle <sup>d</sup>, Volker Uhlenwinkel <sup>a,b</sup>, Lutz Mädler <sup>a,b,\*</sup>

<sup>a</sup> Leibniz Institute for Materials Engineering IWT, Badgasteiner Strasse 3, 28359 Bremen, Germany

<sup>b</sup> University of Bremen, Faculty of Production Engineering, Badgasteiner Strasse 1, 28359 Bremen, Germany

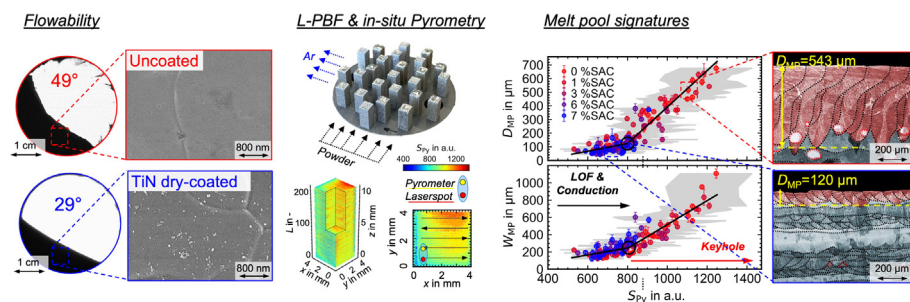
<sup>c</sup> Max-Planck-Institut für Eisenforschung GmbH, Max-Planck-Strasse 1, 40237 Düsseldorf, Germany

<sup>d</sup> Universität der Bundeswehr München, Institute of Materials Science, Werner-Heisenberg-Weg 39, 85577 Neubiberg, Germany

## HIGHLIGHTS

- TiN nanoparticle dry-coating reduced power cohesion of a  $\text{Co}_{25}\text{Cr}_{25}\text{Fe}_{25}\text{Ni}_{25}$  metal powder (20–90  $\mu\text{m}$ ) and enhanced flowability and packing density.
- Dry-coating showed marginal variations of the powder reflection via UV–Vis spectroscopy.
- Thermal emissions from *in situ* confocal single-color pyrometry and *ex situ* solidified melt pool dimensions were predictive of conduction and keyhole fusion mode.
- Enhancing powder processability directly decreased melt pool signatures and significantly shifted keyhole and lack-of-fusion porosities in the  $P$ - $v$ -space.

## GRAPHICAL ABSTRACT



## ARTICLE INFO

### Article history:

Received 6 November 2022

Revised 7 January 2023

Accepted 11 January 2023

Available online 13 January 2023

### Keywords:

Powder flowability

Dry-coating

Laser-powder-bed-fusion

Pyrometry

Melt pool signature

## ABSTRACT

Metal powders in laser-powder-bed-fusion (L-PBF) often exhibit cohesive flow resulting from interparticle adhesion. Nanoparticle dry-coating can improve powder flowability and promote powder layer densification. A  $\text{Co}_{25}\text{Cr}_{25}\text{Fe}_{25}\text{Ni}_{25}$  metal powder (20–90  $\mu\text{m}$ ) is dry-coated with TiN particles with a diameter of 16 nm at low concentrations of up to 69 ppm. The dynamic angle of repose decreased and bulk powder density increased compared to the uncoated state from 49° and 4.67  $\text{g}/\text{cm}^3$  to 29° and 4.81  $\text{g}/\text{cm}^3$  with dry-coating of TiN, respectively. UV/Vis spectroscopy showed negligible alterations by TiN additions on the powder light absorption. The powder modifications strongly affected their corresponding processability in L-PBF and reduced the melt pool signatures of the *in situ* detected confocal single-color pyrometer signal as well as *ex situ* measured melt pool depth and width. With increasing flowability, a significant decrease in thermal emission and melt pool size was observed. The results demonstrate the impact of powder flowability and bulk powder density on the quality of L-PBF parts when particle interactions are actively modified.

© 2023 The Authors. Published by Elsevier Ltd. This is an open access article under the CC BY license (<http://creativecommons.org/licenses/by/4.0/>).

## 1. Introduction

In laser additive manufacturing (AM) processes, such as laser-powder-bed-fusion (L-PBF), particulate raw materials with a

\* Corresponding author.

E-mail address: [lmaedler@iwt.uni-bremen.de](mailto:lmaedler@iwt.uni-bremen.de) (L. Mädler).

size  $< 100 \mu\text{m}$  are prone to detrimental particle interactions and may suffer from low flowability and packing density. A homogeneous and densely filled layer-wise powder deposition is vastly depending on the powder flowability [1]. Nanoparticulate coatings facilitate the improvement of flowability while reducing particle interactions [2]. Qualitative relations of an increased flowability and packing density upon active alteration of particle interactions on the quality of 3D-printed parts has remained largely unexplored.

The processability of particulate materials in L-PBF is a complex function of, amongst other factors, granulometric properties (e.g. particle size and shape distribution), mechanical consolidation stress and particle interactions. Dominant attractive forces can constrain relative motions of particles and induce sever formation of agglomerates. The macroscopic properties of powder flowability and packing density are largely determined by these microscopic interactions [3]. In a dry environment and in the absence of capillary forces, an increased Van der Waals force  $F_{\text{VdW}}$  results in particle adhesion promoting a cohesive flow behavior. Castellanos [4] introduced the ratio of the adhesion force to the weight force  $F_G$ , the granular bond number  $Bo_G = F_{\text{VdW}} / F_G$ , which provides a useful evaluation of the flow behavior. If the adhesion force exceeds the particle weight force with  $Bo_G > 1$  a cohesive flow can be observed. Vice versa, if the weight force increases a freely flowing powder with  $Bo_G < 1$  is often observed. Consequently, coarser particle sizes are conventionally used in L-PBF applications where the flow behavior fails to provide steady process operations [5]. However, the force ratio of initially cohesive powder can also be lowered with reducing the adhesion force. Nanoparticles can be deposited on the metal powder surface for this purpose, for example, via a dry-coating [2] or suspension coating [6] process. The adherent nanoparticles act as artificial roughness and mediate an additional separation distance between particles. The increase in distance results in a decrease in Van-der-Waals force and powder cohesion as a function of surface area coverage (SAC) and nanoparticle size. The reader is referred to Zhu, et al. [7] and Meyer [8] for more detailed discussion on the specific effects of nanoparticle concentration and size.

For the production of metallic components via L-PBF, powders are cyclically deposited in layers with a mechanical raking unit. Owing to a variety of granulometric properties, such as particle size and shape distribution, surface roughness, solid density, etc., metallic powders show significantly different capacities to be processed in thin and dense layers [9]. A stable and robust melting process is favorable for L-PBF to avoid the formation of defects [10]. The direct non-destructive measurement of the powder layer density, layer homogeneity and thickness is a challenging task. With the help of discrete element method (DEM) simulation, micro processes, such as the stress distribution in the bulk material during raking and their influence on the powder layer density can be investigated [11,12]. He, et al. [13] were able to show from DEM simulations for increasing particle cohesion and  $Bo_G$  as well as constant particle size distribution that the powder layer quality is strongly affected. Both local packing density and layer homogeneity decreased as a result of dominant particle adhesion. Chen, et al. [14] numerically investigated the effect of increasing particle surface energy of 316L on the powder layer formation process. Both the dynamic angle of repose, a commonly used measure of powder flowability in metal AM, and the powder bed uniformity were highly dependent on powder cohesion. The number and size of voids increased with cohesive forces. In a second study Chen, et al. [15] investigated the importance of particle size distribution on the density of the powder layer. A significant increase in Van-der-Waals force was found for a 316L steel powder below  $45 \mu\text{m}$ , promoting particle agglomeration and reducing the powder layer density. However, when numerically decreasing particle interac-

tion forces for a given particle size, the powder layer density is drastically increased [14,16–18]. Combining DEM with fluid dynamic modeling of the laser fusion process Cao [19] and Le, et al. [20] both showed that an increasing powder layer density at a constant layer thickness of  $50 \mu\text{m}$  results in smaller melt pool dimensions characteristic to the L-PBF process. Zheng, et al. [21] numerically increased the packing density of Inconel 625 powder with low variations of the layer thickness and reported an increased laser track continuity and a decrease in peak melt pool temperature. This is potentially due to an increase in the total heat of fusion to melt the larger mass of particles per layer. Wei, et al. [22] numerically increased the powder layer density from 0.45 to 0.7 % and found a decreasing melt pool depth. This was attributed to a decrease in melt pool temperature and flow velocity of the melt resulting from increased thermal conductivity of the denser packed powder layer. Increasing the powder layer density without actively altering surface properties has been shown experimentally by Haferkamp, et al. [23] with comparing differently shaped of 316L and AlSi10Mg powders. It was found, that an increased sphericity promotes better flowability and packing behavior. Riener, et al. [24] showed a densification of the powder layer density with increasing fines content for 316L as a result of widening of the particle size distribution and its ability to pack denser.

Nanoparticles offer a variety of useful features for their use in L-PBF. In addition to modifying the powder flow performance and resultant powder layer density, nanoparticles can be used for a variety of beneficial effects, such as mitigating keyhole pore formation, enhancing laser absorption and tuning material properties. For 4.4 vol% TiC nanoparticles (83 nm) ball-milled with an Al6061 metal powder, Qu, et al. [25] showed that an increased melt viscosity through the addition of nanoparticles reduces the keyhole collapse by limiting the evolution of the protrusion and the recovery of the pore through the keyhole. Pannitz, et al. [26] demonstrated for different nanoparticles (few layer graphene, SiC and iron oxide black) in concentrations above 0.75 vol% an increasing laser absorption for aluminum and iron based materials. Also Mair, et al. [27] showed an increasing absorption for the decoration of the 2024 aluminum alloy with 2 wt% nano-CaB6. To enhance the light absorption properties, a sufficiently high concentration of the nanoparticles on the metal powder surface is required. These quantities are several times greater compared to the nanoparticle concentrations needed for the flowability improvement. The user is free to choose the combination of nanoparticles and metal particles, as the flow-enhancing effect of the nanoparticles mainly depends on the particle size ratio. The selected nanoparticles may be beneficial to the material properties of the L-PBF product in addition to improving the processability of the powder. We selected TiN nanoparticles as suitable candidates given that Li, et al. [28] reported the strengthening effect of TiN in a high entropy CoCrFeNiMn alloy.

The present study provides fundamental knowledge of how nanoparticle dry-coating improves the powder flowability and affects the L-PBF processing space. It will be shown that the powder flowability has an extensive effect on *in situ* thermal emission of melt pool as well as *ex situ* measured melt pool dimensions.

## 2. Materials & methods

### 2.1. Metal powder synthesis, powder classification and granulometry

A compositionally complex alloy metal powder of nominal equimolar composition  $\text{Co}_{25}\text{Cr}_{25}\text{Fe}_{25}\text{Ni}_{25}$  was prepared via gas atomization. The atomization process was carried out under Argon atmosphere at  $1680^\circ\text{C}$  including a superheating temperature of  $250^\circ\text{C}$ . The applied synthesis route including a tangential gas sys-

tem to avoid particle recirculation is described in detail by Schwenck, *et al.* [29] and Beckers, *et al.* [30]. The powder fraction 20–90 µm resulted from air-classification at 20 µm (100AFG, Hosokawa Alpine AG) and sieving at 90 µm (MS400, Russell Finex N.V.) under inert gas atmosphere. Particle size distributions of this powder were measured with laser diffraction (Mastersizer 2000, Malvern Instruments GmbH) in an aqueous suspension at 20 °C.

The chemical composition was obtained from optical emission spectroscopy (ICP-OES) (Optima8300, PerkinElmer) for the major metallic elements dissolved in a mixture of HCl and HNO<sub>3</sub>. The oxygen and nitrogen content were determined through carrier hot gas extraction (CGHE) (Fusion Master ONH, NCS Germany) (see Table 1).

## 2.2. Surface modification via nanoparticle dry-coating

Commercially available cubic, nanoscale titanium nitride TiN (CAS No.: 25583-20-4) was purchased from US Research Nanomaterial, Inc. The manufacturer reports a solid density of  $\rho_G = 5.22 \text{ g/cm}^3$ . Nitrogen adsorption measurements (BET) (Autosorb - Quantachrome GmbH & Co. KG) resulted in a mass specific surface area  $S_{\text{BET}}$  of 72 m<sup>2</sup>/g and consequently an average BET nanoparticle size of  $D_{\text{BET}} = 16 \text{ nm}$ . Following a previous study [2], we chose the same experimental set-up as the dry-coating process with SiO<sub>2</sub> nanoparticles (~13 nm). The aggregate size of roughly 100 nm were sufficiently small to promote a reduction in attraction force. For nanoparticle dry-coating, different amounts of TiN nanoparticles were added to approximately 500 g of dried (200 °C for 2 h) metal powder and mixed in a three-dimensional shaker mixer (Turbula T2F, WAB GmbH) at 2 min mixing time and a rotational speed of 101 rpm in a 1 L plastic container. All samples were stored with dry silica pads. The effect of the admixed nanoparticles on powder processability was investigated by varying the nominal surface area coverage (SAC). The calculation of the nominal surface area coverage of nanoparticles is based on a theoretical concept described by Meyer and Zimmermann [31]. According to their study SiO<sub>2</sub> nanoparticles can be arranged geometrically stable in a square or hexagonal lattice on a cornstarch carrier particle when dry-coated. The densest arrangement was found for the hexagonal configuration. The SAC then can be calculated using Equation (1) and (2), where  $S_{\text{NP}}$  is the projection area of the primary nanoparticles,  $D_{\text{NP}}$  the nanoparticle diameter (16 nm),  $N_{\text{NP}}$  the total number of nanoparticles used, and  $S_M$  the mass-related surface area of the metal powder ( $S_M = 0.0186 \text{ m}^2/\text{g}$  in this study).

$$\text{SAC} = \frac{S_{\text{NP}} \cdot N_{\text{NP}}}{S_M} \quad (1)$$

$$S_{\text{NP}} = \frac{\sqrt{3}}{2} D_{\text{NP}} \quad (2)$$

The effect of increasing nanoparticle concentration on powder flowability and L-PBF processing was investigated for TiN surface area coverages from 0, 1, 3, 6 and 7 %SAC and corresponding mass fractions of 0, 10, 32, 58 and 69 ppm.

**Table 1**

Chemical composition of the metal powder.

Element	Co	Cr	Fe	Ni	Ti	N	O
wt-%	25.9	22.4	25.95	25.7	<0.001	0.037	0.017
at-%	24.7	24.3	26.2	24.6	<0.001	0.149	0.060

## 2.3. Surface characterization (SEM) and powder reflectance measurements (UV/Vis)

A Supra40 (Zeiss) scanning electron microscope (SEM) equipped with Inlense and secondary electron detectors was used to acquire images of the metal powders. The surface and morphology characterizations were performed at an accelerating voltage of 2 kV (Inlense) and 7 kV (SE) and a working distance of 2.9 mm (Inlense) and 7.1 mm (SE).

Powder reflectance measurements were performed with an ultraviolet/visible light (UV/Vis) spectrophotometer (UV-2600, Shimadzu GmbH) at a wavelength ranging from 185 to 1400 nm in triplets. Baseline measurements were performed on a powdered BaSO<sub>4</sub> reference. Approximately 3 g of the powder samples were placed in a powder sample container and closed with a glass plate for the integrating sphere attachment. The powder layer thickness in the powder container was several millimeters, and significantly larger compared to realistic L-PBF process conditions.

## 2.4. Powder flowability and density characterization

Measurements of the dynamic angle of repose  $\alpha$  and Hausner ratio  $HR$  were employed to determine the effect of nanoparticle dry-coating on the powder flowability and packing. The dynamic angle of repose  $\alpha$  was deduced from measuring the inclined angle before an avalanche occurred of 25 g powder at rotation speed of 5 rpm in a self-designed device. The Hausner ratio  $HR$ , the quotient of the freely settled bulk powder density  $\rho_B$  to tapped powder density  $\rho_T$ , was measured freely pouring the powder sample into a 10 ml flask of a tapping volumeter (STAVII, Engelsmann AG). The manual reading of the pile surface was conducted before and after tapping 1250 times with the device.

## 2.5. Sample preparation via L-PBF and in situ pyrometry

L-PBF experiments were carried out with a commercially available system (Aconity Mini, Aconity3D GmbH) equipped with a single-mode fiber laser ( $P_{\text{max}} = 400 \text{ W}$ ) at an operating wavelength of  $\lambda = 1064 \text{ nm}$ . For each nanoparticle concentration, 25 specimens with a geometry of 4x4x10 mm<sup>3</sup> (=200 layers) were produced. The laser power and scan velocity were varied between 100 and 350 W and 0.2–1.0 mm/s, respectively. A 90 ° rotating scan pattern of alternating tracks was chosen to prepare samples with constant laser spot diameter 90 µm, hatch distance 70 µm and nominal powder layer thickness of 50 µm. Powder layers were deposited via a carbon fiber brush at a deposition velocity of 100 mm/s perpendicular to an Argon inter gas flow. All experiments were performed below 60 ppm O<sub>2</sub> content and at 50 mbar overpressure.

L-PBF process signatures, such as melt pool radiation, have been successfully related with defect structures [32,33]. Forien, *et al.* [34] correlated the melt pool radiation of an uncalibrated, confocal *in situ* single-color pyrometer and *ex situ* X-ray radiography with melt pool dimension. The transition from conduction to keyhole fusion mode of a 316L steel powder was identified and the onset of the keyhole instability was found in close agreement with the findings of King, *et al.* [35]. A single-color pyrometer (KG740, Kleiber Infrared GmbH) assembled confocally to the incident laser enabled pyrometric emission monitoring of the welding process

at a wavelength of  $\lambda = 1560 \pm 100$  nm and acquisition frequency of 100 kHz. The experimental set-up with the *in situ* pyrometric monitoring assembled confocally with working laser is shown schematically in [Supplementary Fig. S1](#). The process monitoring was used uncalibrated with regard to true temperature measurements as relative correlations only between metal powders of similar chemistry were investigated. For more details of the *in situ* pyrometric experimental set-up the reader is referred to Gaikwad, *et al.* [33] and Forien, *et al.* [34], Forien, *et al.* [36]. Thermal emissions in form of the digital pyrometer signal  $S_{\text{py}}$  were collected from the melt pool. The broad field-of-view of  $\sim 1$  mm in diameter was displaced in positive y-position by  $\sim 500$   $\mu\text{m}$  of the laser spot (see [Fig. 5](#)). The rotating scan pattern therefore resulted in four different measurement situations, where the pyrometer spot was ahead, behind or aside from the laser scan track. The positioning was kept constant throughout all L-PBF experiments. The lowest value of the pyrometer signal measured over 200 layers of each specimen was subtracted from all collected data to account for signal noise at room temperature.

### 2.6. Metallography

The specimens were removed from the baseplates through wire electric discharge machining, embedded and polished in x-direction until half of sample ( $\sim 2$  mm) was removed. Porosity measurements were carried out with an automatic light microscope (Axio, Carl Zeiss Jena GmbH) at a magnification of  $x10$  (1.8 pixel/ $\mu\text{m}$ ) and binarized image analysis with the free software ImageJ/Fiji. Electrolyte etching with V2A etchant revealed the dimensions of the solidified melt pools of the last laser exposed layer. Manually reading of at least five melt pools per specimen with ImageJ/Fiji resulted in the melt pool depth  $D_{\text{MP}}$  and width  $W_{\text{MP}}$  analysis.

## 3. Results & discussion

### 3.1. The effect of TiN nanoparticle dry-coating on powder processability and light absorption

In this study a compositionally complex alloy  $\text{Co}_{25}\text{Cr}_{25}\text{Fe}_{25}\text{Ni}_{25}$  powder was prepared using gas atomization and subsequent powder classification. The corresponding particle size distributions  $Q_3$  and  $q_3$  are shown in [Fig. 1-a](#). The powder classification processes resulted in a powder of mean Sauter diameter of  $D_{1,2} = 38 \mu\text{m}$  with fine content  $< 20 \mu\text{m}$  of 8 vol%. With characteristic distribution values of  $D_{10,3} = 22 \mu\text{m}$ ,  $D_{50,3} = 46 \mu\text{m}$  and  $D_{90,3} = 85 \mu\text{m}$  this particle size range is considerably coarser compared to conventional L-PBF powders, typically sieved  $< 63 \mu\text{m}$ . The synthesis of the  $\text{Co}_{25}\text{Cr}_{25}$

$\text{Fe}_{25}\text{Ni}_{25}$  metal powders through gas atomization yielded a predominantly spherical particle morphology free from adhering satellite structures ([Fig. 1-b](#)). The aggregated TiN nano particles used for dry-coating are shown in [Fig. 1-c](#). The surface of a  $20 \mu\text{m}$  metal particle with a nominal TiN nanoparticle surface area coverage of 6 %SAC is shown as an example in [Fig. 1-d](#). A uniform distribution of aggregated nanoparticles can be seen on the surface of the metal particle.

Successful layer-by-layer spreading of homogeneous metal powder layers requires good flowability [5]. Particle interactions often result in cohesive flow based on strong attractive forces. Nanoparticle dry-coating provides a method of reducing such interactions. [Fig. 2](#) illustrates the effect of TiN deposition on the metal powder surface through dry-coating of the  $\text{Co}_{25}\text{Cr}_{25}\text{Fe}_{25}\text{Ni}_{25}$  powder and the resulting flow behavior using drumflow snapshots and funnel outflow images. Increasing the nanoparticle concentration from 0 to 7 %SAC resulted in an increased number of nanoparticles on the naturally rough metal powder surface. Dry-coating caused an assembly of almost homogeneously distributed nanoparticle aggregates. The nanoparticles can adhere on the metal powder surface as well as to each other based on multiple interactions. The coating procedure was performed under ambient conditions with relative humidity above zero. These conditions can result in the water vapor condensation on the nanoparticle surface forming a structured water molecular layer [37]. The resulting capillary force and Van-der-Waals force dominate the adhesion between nanoparticle and metal particle [38]. The addition of small amounts of TiN resulted in an improvement of the flow properties. Lower avalanche angles and smoother outflow patterns were observed at a TiN surface area coverage  $\geq 3$  %SAC.

The observed improvement on the powder flowability due to TiN dry-coating is supported with measurements of the dynamic angle of repose  $\alpha$  and bulk powder density  $\rho_B$  and tapped powder density  $\rho_T$ . [Fig. 3-a](#) shows a reduction of the dynamic angle of repose with increasing surface area coverage. Dry-coating resulted in a reduction of the dynamic angle of repose of the uncoated powder of  $49 \pm 3^\circ$  towards  $32 \pm 2^\circ$  and  $29 \pm 1^\circ$  at 3 and 7 %SAC. The bulk powder density increased from  $4.67 \pm 0.06 \text{ g/cm}^3$  to  $4.79 \pm 0.07 \text{ g/cm}^3$  and  $4.81 \pm 0.08 \text{ g/cm}^3$ , whereas the tapped powder density decreased less strong from  $5.45 \pm 0.04 \text{ g/cm}^3$  to  $5.41 \pm 0.13 \text{ g/cm}^3$  and  $5.39 \pm 0.04 \text{ g/cm}^3$ . A statistically significant increase in bulk powder density upon TiN nanoparticle dry-coating between 0 and 7 %SAC was confirmed using the statistical *t*-test ( $t = -4.2$ ,  $p = 0.002$ ).

The classification according to Carr [39] and Riley and Hausner [40] provides a useful evaluation of the processability with comparing  $\alpha$  and  $HR$  as the ratio of freely settled bulk to tapped powder density in [Fig. 3-b](#). As both the dynamic angle of repose and Haus-

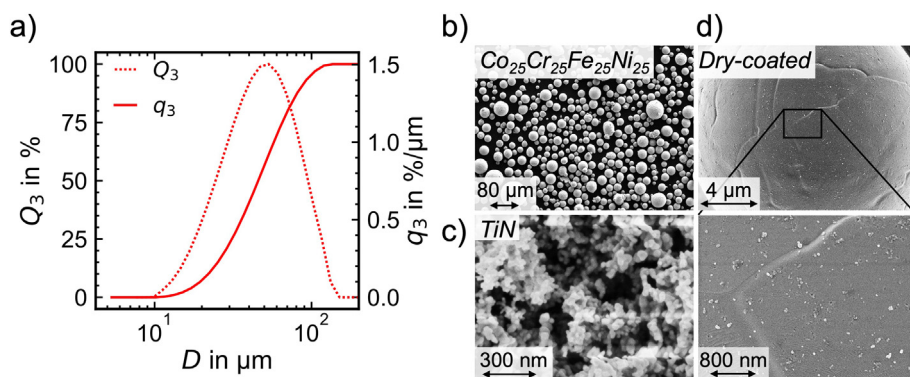


**Fig. 1.** Particle size distributions  $Q_3$  and  $q_3$  and SEM micrograph of the  $\text{Co}_{25}\text{Cr}_{25}\text{Fe}_{25}\text{Ni}_{25}$  metal powder (a) and (b), (c) nanosized TiN bulk powder, (d)  $20 \mu\text{m}$  particle dry-coated with 6 %SAC TiN.

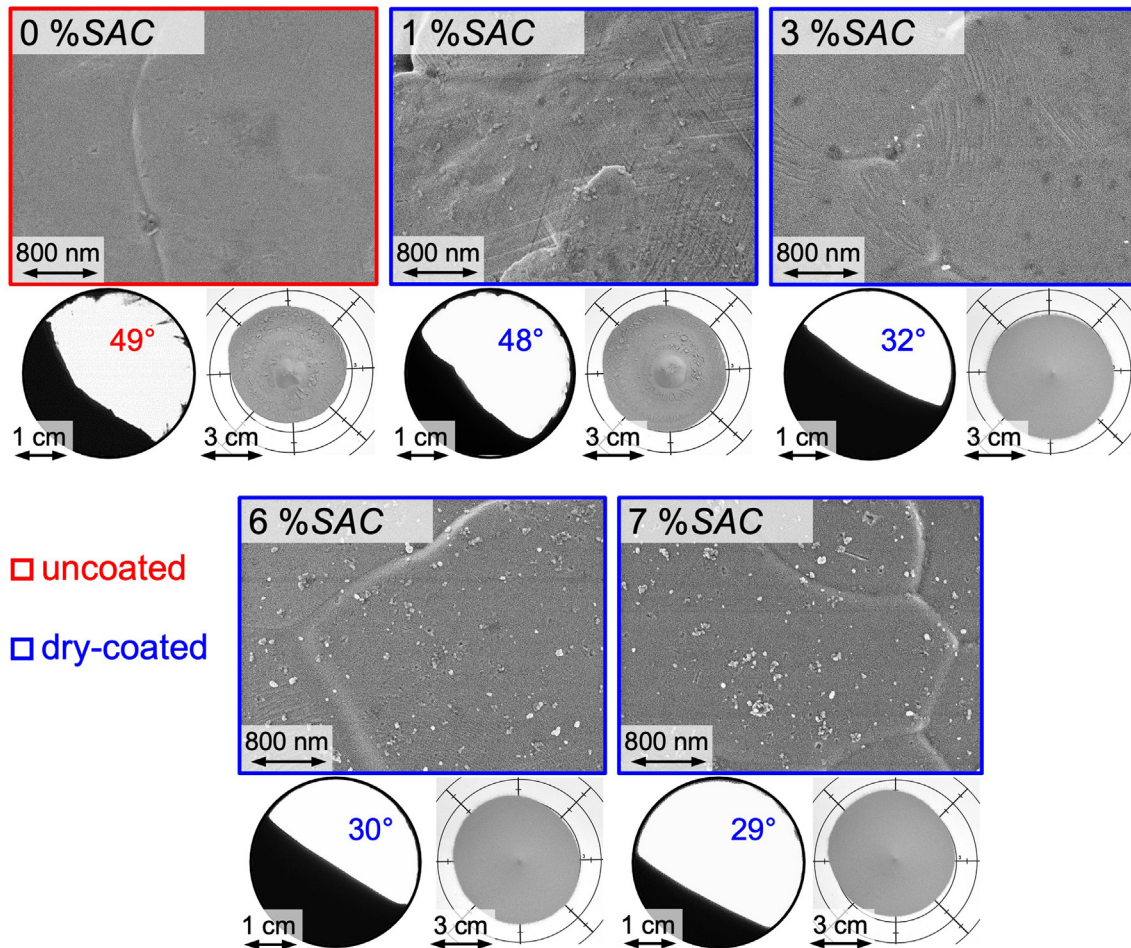


**Fig. 2.** Qualitative SEM images of the TiN dry-coated  $\text{Co}_{25}\text{Cr}_{25}\text{Fe}_{25}\text{Ni}_{25}$  particle surfaces, drumflow snapshots compared to funnel outflow images at surface area coverages SAC from 0 to 7 % SAC.

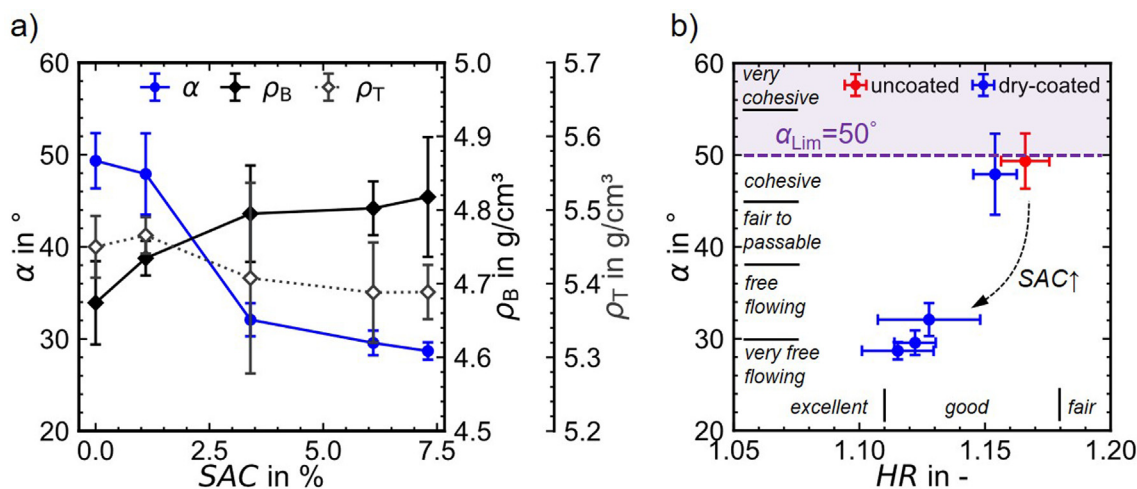


**Fig. 3.** Effect of nanoparticle dry-coating on powder flowability and packing - (a) Dynamic angle of repose  $\alpha$  and bulk powder density  $\rho_B$  and tapped density  $\rho_T$  vs nominal TiN surface area coverage SAC and (b) comparison between  $\alpha$  and HR with indications of the powder processability according to Carr [39] and Riley and Hausner [40].

ner ratio decreased from 49° and 1.17 (0 %SAC) to 29° and 1.11 (7 %SAC) upon nanoparticle dry-coating a clear improvement in powder processability is observed. A limiting dynamic angle of repose  $\alpha_{\text{Lim}} = 50^\circ$  was defined as the minimum necessary angle of repose for homogeneous powder coating in L-PBF applications [2]. With a

dynamic angle of repose of 49°, the uncoated powder was successfully L-PBF processed. With increasing nanoparticle concentration an increase in flowability from “cohesive” to “very free flowing” was determined and increasing packing density is seen. The results of *ex situ* measured flowability and packing density are in close

agreement with the findings of DEM simulations reported by several authors [1,14,16,17]. Haferkamp, *et al.* [23] further demonstrated that a decreasing Hausner ratio is associated with an increasing powder layer density. It can be expected that the powder layer density increases with improving flowability and packability by reducing the powder cohesion as a result of decreasing particle adhesion forces. However, during the actual layer formation, parameters such as the coater geometry used [41], the deposition velocity [42] and the roughness of the previously melted layer [9] will affect the powder layer density.

Apart from the flowability and packing analyses, nanoparticles are known to increase laser absorption in L-PBF [43]. As low amounts (<69 ppm) of TiN nanoparticles were introduced to the metal powder, which could potentially influence laser absorption, UV-Vis spectroscopy measurements were performed to account for the possible variation in the laser-metal interaction. Fig. S2 shows the reflection spectra of pure TiN bulk powder and the dry-coated  $\text{Co}_{25}\text{Cr}_{25}\text{Fe}_{25}\text{Ni}_{25}$  metal powders. At the laser wavelength of a L-PBF machine of  $\lambda = 1064$  nm pure TiN exhibited low reflectivity of  $\sim 1\%$  and thus high absorptivity when transmission is assumed to be zero. However, statistically irrelevant differences in the reflectance of the metal powders from  $35.4 \pm 0.1\%$  to  $34.4 \pm 0.6\%$  were observed with a dry-coating of 0 to 7 %SAC. Consequently, TiN nanoparticle surface coating of up to 7 %SAC has a neglectable effect on the powder laser absorption. Existing studies targeting enhanced light absorption properties by nanoparticle coating, such as Pannitz, *et al.* [26] and Mair, *et al.* [27] use 80 to 200 times higher nanoparticle concentration compared to the maximum concentration of our study. In the selected concentration range < 69 ppm, the TiN nanoparticles showed negligible effect on the light absorption of the metal powders in our study. Therefore, it can be concluded that the results of the L-PBF process performance presented subsequently is not noticeably affected by the laser absorption of the nanoparticle coating.

### 3.2. Melt pool signatures and L-PBF part porosity of uncoated powders

The benchmark results of part porosity and melt pool size of the L-PBF processed uncoated  $\text{Co}_{25}\text{Cr}_{25}\text{Fe}_{25}\text{Ni}_{25}$  reference powder are given in Fig. 4. At laser powers between 200 and 350 W keyhole porosities  $> 4\%$  resulted from a long laser-material interaction time with scan velocities between 0.2 and 0.6 m/s (see Fig. 4-a and -b). Higher scan velocities decreased the porosities below 1 %. At a low laser power of 150 W both keyhole and lack-of-fusion porosities were found, as an increased pore content of 10.9 % resulted from short laser interaction time. *Ex situ* measured melt pool signatures such as the melt pool depth  $D_{MP}$  [44–46] indicate the underlaying mode of fusion. An increasing melt pool depth was found for both increasing laser power and decreasing scan velocity. A deep narrow vapor cavity is created at the bottom of the melt pool in the keyhole regime increasing the energy absorption through multiple reflections in the cavity [47]. The uncontrolled collapse of this cavity leads to an enclosed, often circular vapor pore detrimental to the performance of the part [48]. Vice versa, at low energies, the metal powder is melted incompletely (lack-of-fusion) and powder voids and unfused areas remain [49]. Fig. 4-c shows the transition of the unstable keyhole regime (cavities at the bottom) to conduction melting (low porosity) with decreasing scan velocities based on binarized cross-sectional porosity and metallographic images of the melt pools at  $P = 250$  W. The melt pool depth  $D_{MP}$  of the part top layer gradually decreased with scan velocities of 0.3, 0.6 and 1.0 m/s at  $P = 250$  W from  $543 \pm 43$   $\mu\text{m}$ , to  $350 \pm 25$   $\mu\text{m}$  and  $151 \pm 13$   $\mu\text{m}$  respectively. A low porosity content < 0.1 % was observed in the range of 200–350 W and 0.8–1.0 m/s.

Fig. 5 summarizes the procedure of data acquisition with the applied *in situ* single-wavelength pyrometric monitoring of the thermal emissions at 0 %SAC TiN nanoparticle concentration. Over the course of producing 25 samples in 200 layers the pyrometer spot was confocally aligned to the operating laser with a displacement of  $\sim 500$   $\mu\text{m}$  in positive y-positions and field-of-view of  $\sim 1$  mm. The rotating and alternating scan pattern resulted in four different measurement situations repeating every fifth layer (see Fig. 5-b). Whenever the pyrometer spot traveled in front or behind the operating laser, thermal emissions were lower compared to when placed parallel to the scan path. The high temporal resolution of the pyrometer enables the detection of specific pyrometer signal variations. In each layer a heat accumulation along the proceeding scan tracks is observed from an increasing thermal radiation. This results in a high variation of the average signal within each layer illustrated in Fig. 5-c and -b. The average pyrometer signal  $S_{Py}$  in arbitrary units (a.u.) of every fourth layer with respect to the layer number  $L$ . At a constant laser power of  $P = 250$  W and varying scan velocities the pyrometer signal increases in z-direction of the L-PBF sample (Fig. 5-c). At the constant laser power and decreasing scan velocity from 1.0 m/s to 0.3 m/s, the average pyrometer signal and standard deviation increase from  $816 \pm 97$  a.u. to  $1105 \pm 144$  a.u. as a result of the elevated laser energy density. An increasing pyrometer signal across component height can be assigned to the heating of the sample in the course of successive layer melting. The scattering of the signal may enable further investigations to draw conclusions about distinct process features. The thermal emission from the melt pool showed to be specific for a given  $P$ -v-combination. The pyrometric signal  $S_{Py}$  is therefore considered a thermal melt pool signature resembling the fusion history of each layer during L-PBF. In combination with a metric resembling the melt pool size, the signal of the *in situ* pyrometric measurement can be used to predict a change in laser-matter interaction.

### 3.3. The effect of TiN nanoparticle dry-coating on melt pool signatures and L-PBF part porosity

Fig. 6-a shows the porosity and melt pool size analysis for varying scan velocities  $v = 0.2\text{--}1.0$  m/s and increasing SAC at  $P = 200$  W, where the internal porosity defects are most pronounced. Increasing the surface area coverage from 0 to 1 and 7 %SAC resulted in a decrease in porosity from 10.1 % to 7.8 % and 0.6 % at a scan velocity of 0.2 m/s and corresponding high energy density. A reverse effect is observed for shorter laser interaction times. With increasing nanoparticle concentration, the porosity increased from 0.06 % to 0.24 % and 4.7 % at  $v = 1.0$  m/s. At a scan velocity of  $v = 0.2$  m/s, the melt pool depth  $D_{MP}$  decreased from  $450 \pm 11$   $\mu\text{m}$  (0 %SAC) to  $166 \pm 65$  (7 %SAC). Smaller differences between  $121 \pm 6$   $\mu\text{m}$  (0 %SAC) and  $61 \pm 8$   $\mu\text{m}$  (7 %SAC) were measured at a high scan velocity  $v = 1.0$  m/s. Increasing the nanoparticle concentration consequently resulted in a less pronounced keyhole and conduction fusion mode as the melt pool depth reduced in size. As the TiN nanoparticle coating showed insignificant variations of laser absorption of the powders, the reduction in melt pool size appears likely to be associated with the enhanced powder processability. The enhanced flowability and powder bulk density suggest an increased powder layer density. At a constant energy density  $P/v^{0.5}$ , a higher solid fraction per layer will have to be melted as the nanoparticle loading increases. This results in consistently lower melt pool depths compared to the uncoated powder. The energy density required to develop the conduction or keyhole fusion mode thus appears to be specific to the TiN surface coverage and the powder bulk density, respectively. In addition, it can be assumed that there are fewer voids in the powder layer due to the lower powder cohesion. The increased powder layer homo-

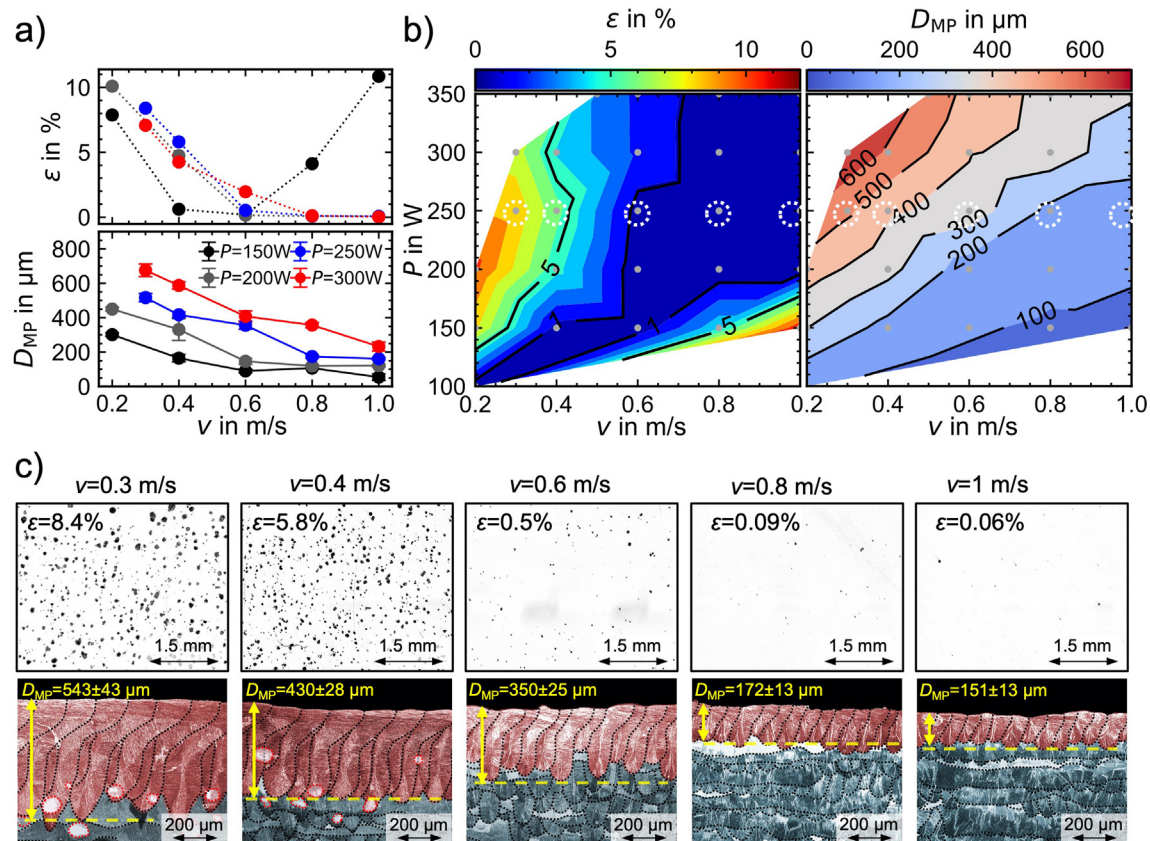


**Fig. 4.** Metallographic properties of L-PBF processed uncoated  $\text{Co}_{25}\text{Cr}_{25}\text{Fe}_{25}\text{Ni}_{25}$  – (a) comparison of porosity  $\varepsilon$  and melt pool depth  $D_{MP}$  upon selected laser power  $P$  and scan velocities  $v$ ; (b) summarized results of  $\varepsilon$  and  $D_{MP}$  in the chosen  $P$ - $v$ -space (grey circles = L-PBF sampling points); (c) transition from keyhole to conduction fusion mode via exemplary light microscopy images of the L-PBF part porosity (binarized) and top layer melt pool dimensions at  $P = 250$  W indicated with white circles in the  $P$ - $v$ -space of (b).

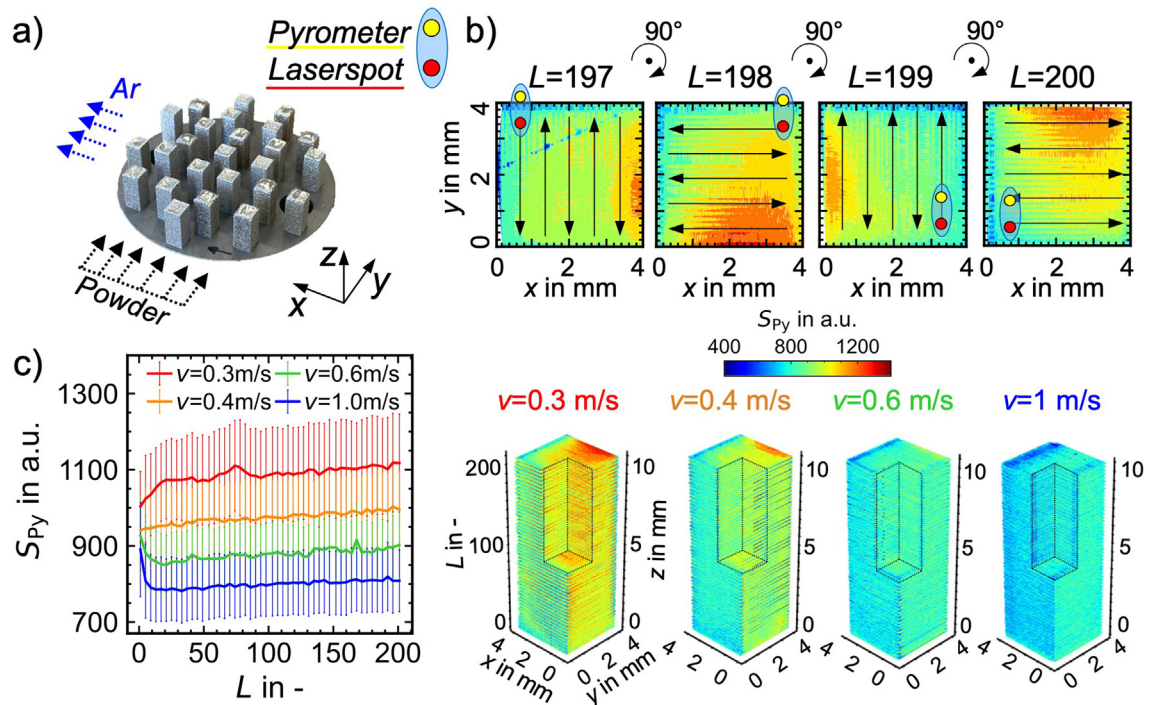


**Fig. 5.** L-PBF *in situ* pyrometric measurement of uncoated  $\text{Co}_{25}\text{Cr}_{25}\text{Fe}_{25}\text{Ni}_{25}$  – a) acquisition of 25 samples ( $4 \times 4 \times 10$  mm) per powder; b) alternating and  $90^\circ$  rotating scan strategy and pyrometer alignment (top row), layer reconstruction of pyrometer signal  $S_{Py}$  and indicated scan vectors at 250 W and 0.3 m/s; c) evolution of pyrometric signal with increasing layer number  $L$  and 3D signal reconstructions of 250 W and increasing scan velocities between 0.3 and 1.0 m/s.

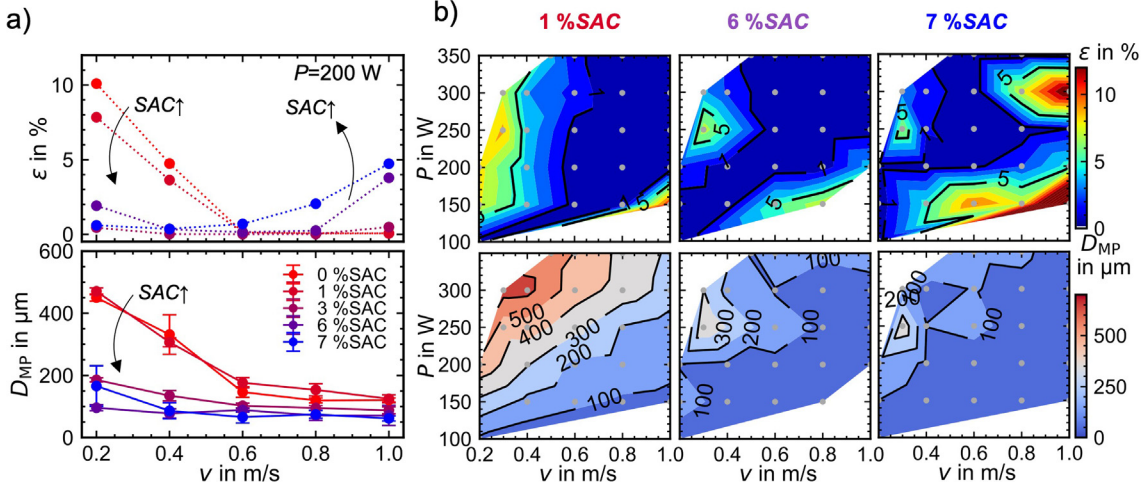


**Fig. 6.** Comparative analysis of the L-PBF part defects and melt pool size upon TiN dry-coating (0 to 7 %SAC) - (a) porosity  $\varepsilon$  and melt pool depth  $D_{MP}$  evolution with increasing scan velocity  $v$  at constant laser power  $P = 200 \text{ W}$  and (b) full  $P$ - $v$ -space analysis (grey circles = L-PBF sampling points).

geneity leads to smaller melt pool fluctuations and a reduction of deep laser penetration caused by the absence of particles ahead of the wetting front of the melt pool. Fig. 6-b shows the complete analysis of the  $P$ - $v$ -space at 1, 6 and 7 %SAC. In the high energy region of the  $P$ - $v$ -space with medium to high laser power and low scan velocities, a reduction of the keyhole porosity and melt pool depth with the addition of nanoparticles is observed. On the contrary, in the low energy region with low to medium laser power and high scan velocities a pronounced lack-of-fusion porosity is observed. The insufficient powder melting resulted in an incomplete bonding with previous layers. The porosity regions of keyhole and lack-of-fusion detrimental to the L-PBF part quality shifted towards higher energies was observed. The shift of internal part defects resulted from the reducing melt pool depth upon the addition of TiN nanoparticles.

Fig. 7-a shows the calculated average pyrometer signal of all printed parts over the entire sample height, reduced by the signal noise at room temperature, with different nanoparticle SAC as a function of laser energy density  $P/v^{0.5}$ . For the uncoated powder at 0 %SAC the pyrometric signal  $S_{Py}$  increases in a linear fashion with the laser energy density. With increasing TiN nanoparticle concentration, the slopes of the linear regressions decrease. The corresponding Pearson correlation coefficients  $r$  are positive in all cases, but decrease with increasing nanoparticle concentration,

indicating stronger deviations from the linear behavior. From Supplementary Fig. S3 an increased mean signal of the melt pool emission is accompanied with higher standard deviations. The change in the slope of pyrometric signal to energy density with increasing TiN surface area coverages is shown in Fig. 7-b. At 1 %SAC a slight increase in thermal response of the melt pool is observed. Further increasing the nanoparticle concentration results in a plateau of the slope above 6 %SAC. As the amount of nanoparticles increases, the emitted radiation of the melt pool decreases. This indicates a decrease in temperature and melt pool size, such as melt pool depth. The recorded pyrometer signal is an integral reading of the spatial radiation intensity profile along the melt pool surface. The surface temperature of the melt pool varies axially and radially with the length and width of the melt pool and the penetration depth of the laser (e.g. keyhole), resulting in the melt pool depth. A mean pyrometric value can be assigned to a current melting mode as it captures the total surface radiation of the melt pool. The nanoparticle coating requires a significantly higher laser energy input to maintain the same melt pool signature. This is in close agreement with the effect of nanoparticle dry-coating on the evolution of melt pool depth. The melt pool signatures of *in situ* pyrometer signal  $S_{Py}$  and *ex situ* melt pool depth  $D_{MP}$  decrease with increasing TiN concentration and lead to a substan-

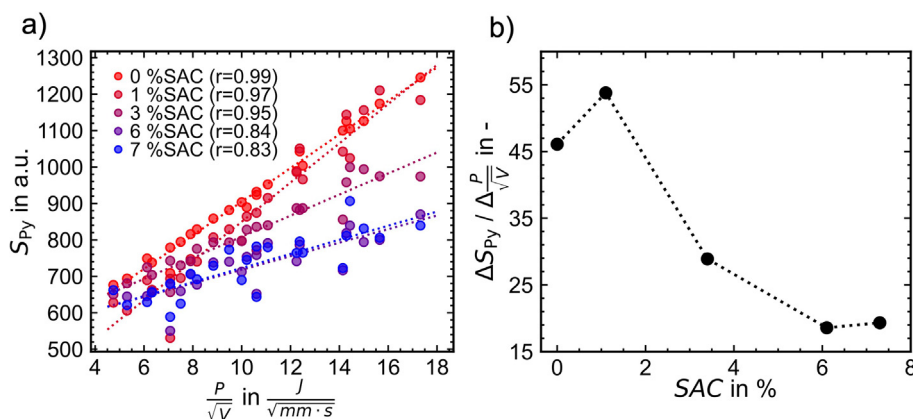


**Fig. 7.** *in situ* L-PBF pyrometric monitoring of 0 to 7 %SAC TiN dry-coated  $\text{Co}_{25}\text{Cr}_{25}\text{Fe}_{25}\text{Ni}_{25}$  powders - (a) mean pyrometer signal  $S_{Py}$  of 200 layers (10 mm build height) as function of process parameter  $P/v^{0.5}$  with Pearson correlation coefficients  $r$  of the linear regressions (the standard deviation was omitted for visual clarity); (b) Slope of pyrometric response of  $\Delta S_{Py} / \Delta P / v^{0.5}$  vs TiN nanoparticle surface coverage.

tial shift in porosity regions towards higher energy densities was found with increasing nanoparticle SAC.

Fig. 8-a shows the results of the melt pool depth  $D_{MP}$  and width  $W_{MP}$  as a function of the mean pyrometric signal upon the laser exposure in the chosen  $P$ - $v$ -space of all TiN concentrations. Two distinct regions in which the fusion mode transitions from conduction to stable and later unstable keyhole mode with increasing thermal emission of the melt pool were found. In the first region ( $<S_{Py} \sim 800$  a.u.) conduction melting resulted in commonly observed lack-of-fusion porosities and dense specimens with a melt pool depth and width lower than 123  $\mu\text{m}$  and 250  $\mu\text{m}$  [35]. With increasing pyrometer signal a distinct change in slope was found for the melt pool depth depicting the onset of the keyhole fusion regime. Both the melt pool size as well as the melt pool shape changed from semi-circular to keyhole-like in Fig. 8-b. The threshold only accounts for the difference of the conduction to key-hole melting. Instable keyhole fusion with impinged vapor cavities are observed for values far higher than the threshold. The uncoated powder with 0 %SAC shows pronounced melt pool dimensions in the conduction and keyhole regions. The addition of nanoparticles results in a reduced pyrometer signal and melt pool depths and widths. Coating with 7 %SAC results in a significant shift of the melt pool dimensions into the conduction fusion mode and a reduction in porosity. At a constant laser heat inflow  $Q$  an increase in powder mass  $\Delta m$  per layer may lead to a decreasing melt pool temperature  $T_{MP} = Q/(m + \Delta m) \cdot c_p + T_0$  at a given heat capacity  $c_p$ , ambient temperature  $T_0$  and powder mass  $m$ . The melt pool temperature and pyrometer signal therefor decrease with increasing nanoparticle concentration and bulk powder density, respectively. This vastly simplified analogy of the complex thermal phenomena of the L-PBF process may explain the reduction of the thermal emission upon nanoparticle dry-coating in concentrations  $< 69$  ppm. Rauniyar and Chou [50] provide another potential explanation, in which any kind of void in the powder bed results in an enhanced downward fluid convection, thereby temporally increasing the melt pool depth. Through actively reducing powder cohesion via nanoparticle dry-coating the void fraction and particle spacing will decrease

and may result in a reduced downward convection and melt pool depth. With reducing the particle adhesion, powder bed voids can be reduced from tighter packing, resulting in less fluctuation of the melt pool. The gradient at which melt pool depth and width increased with the mean pyrometric signal were  $\Delta D_{MP}/\Delta S_{Py} = 1.34$  and  $\Delta W_{MP}/\Delta S_{Py} = 1.38$  with Pearson correlation coefficients of 0.86 and 0.89, respectively. Supplementary Fig. S4 depicts a linear relationship between the melt pool dimension with  $r = 0.91$  underlining similar contribution to the pyrometric signal. The correlation between the thermal emission from the melt pool and the ex situ measured melt pool depth and width indicate that the transition from conduction to keyhole melting depends on the temperature reached in the melt pool. This is in very good agreement with the findings of Hann, et al. [51], King, et al. [35] and Forien, et al. [34] where the input energy of the laser exceeds the boiling point of the materials.

Chen, et al. [52] carried out *in situ* and operando synchrotron X-ray imaging measurements in realistic L-PBF conditions as a multi powder layer set-up was used. It was hypothesized that the increasing melt evaporation rate within the keyhole results from regions of low particle packing ahead of the advancing melt pool wetting front towards the powder. This leads to a reduction in the contact area with the powder surface, the effective laser absorption and the thermal conductivity of powders with low packing. Powders with reduced attractive interactions may more easily spread in denser layers, compensating for regions of low local powder packing. As the powder layer density potentially increases the mass per layer, a higher laser density is required for complete melting. A similar view was presented by Zheng, et al. [21] where lattice Boltzmann simulations of L-PBF processing of Inconel 625 alloy showed a reduction of the melt pool peak temperature from increasing powder packing density. We hypothesize that the increase in necessary melting enthalpy from increased powder packing results in lower thermal emissions as well as smaller melt pool dimensions. Thus, the selection of the process parameters is significantly determined by the metal powder configuration in a powder layer. The results indicate that L-PBF specific

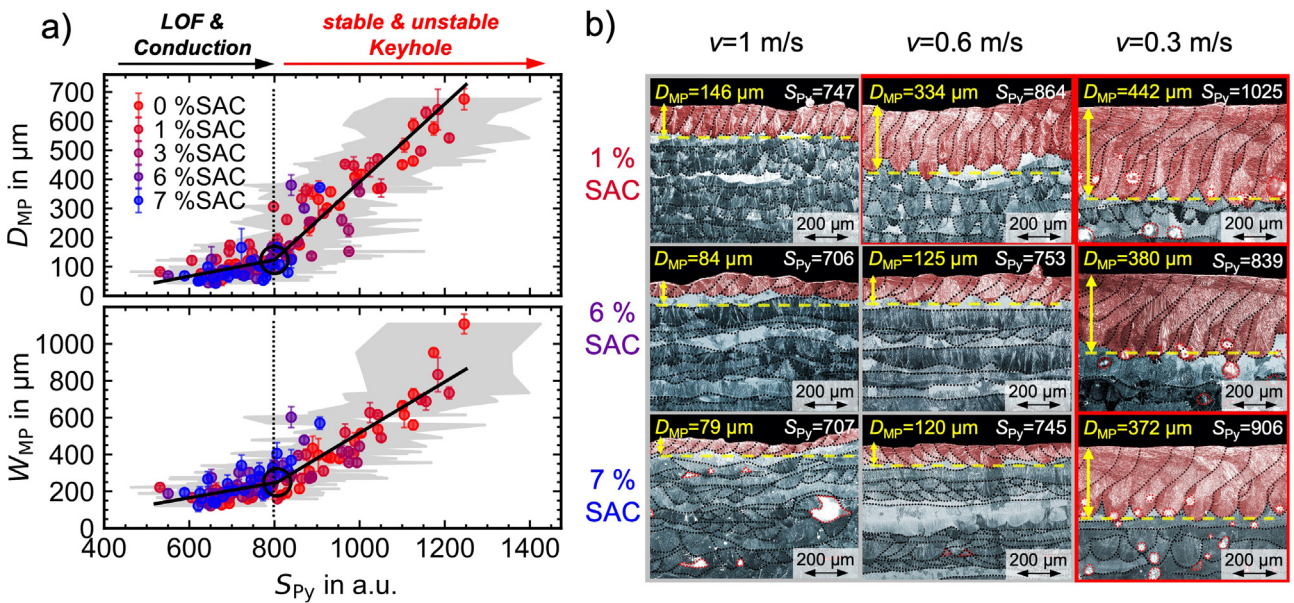


**Fig. 8.** Pyrometric and metallographic analysis of TiN dry-coated  $\text{Co}_{25}\text{Cr}_{25}\text{Fe}_{25}\text{Ni}_{25}$  fractions with increasing TiN surface area coverages – (a) Melt pool depth  $D_{MP}$  (top) and width  $W_{MP}$  (bottom) vs mean pyrometer signal  $S_{Py}$  with the standard deviation as greyed area (qualitative distinction between conduction melting with lack-of-fusion (LOF) and keyhole melting represented via a dashed vertical line  $S_{Py} = 800$  a.u.) and (b) highlighted top layer melt pool morphology (red frame ~ keyhole / grey frame ~ conduction) of 1, 6, and 7 %SAC with indications of melt pool depth  $D_{MP}$  and corresponding mean pyrometer signal  $S_{Py}$  for decreasing scan velocity  $v = 1.0, 0.6$  and 0.3 m/s at the laser power  $P = 250$  W. (For interpretation of the references to color in this figure legend, the reader is referred to the web version of this article.)

porosity regions and fusion modes are both material- but also powder formation specific with the assumption that low nanoparticle concentration of < 69 ppm imply negligible effects on fluid- and thermodynamics.

The addition of nanoparticles changes the chemical composition of the metallic alloy processed via L-PBF. However, the amount of nanoparticles required to improve the processability of powders is comparatively small with respect to the commonly accepted impurity levels. In the present study 70 ppm of TiN nanoparticles showed a drastic improvement of the powder processability and stabilization of the L-PBF process. The amount of nanoparticles is unlikely to affect the thermophysical properties of the alloy. The effect of reducing interparticle forces mainly relies on the size of the nanoparticles, less on the chemical composition of the additives and is therefore applicable to any other alloy.

## 4. Conclusions

In this study, a Co<sub>25</sub>Cr<sub>25</sub>Fe<sub>25</sub>Ni<sub>25</sub> metal powder (20–90 µm) was dry-coated with 16 nm sized TiN nanoparticles in different concentrations and processed in a L-PBF machine to investigate the applicability of dry-coated powders and to correlate melt pool signatures. Dry-coating with nanosized TiN reduced the dynamic angle of repose from 49 ° to 29 ° with TiN concentrations of <69 ppm. The assessment of the Hausner ratio as a measure of the packing behavior showed a significant improvement of all dry-coated powders. UV-Vis reflectance measurements of the powders coated with highly absorbing TiN showed a negligible effect on the absorptivity at the operating wavelength of the L-PBF laser  $\lambda = 1064$  nm.

Applying nanoparticle dry-coated metal powders to the L-PBF process resulted in a shift of the lack-of-fusion and keyhole porosity regions. Using *in situ* thermal emission measurements via confocal pyrometry, the fusion modes of conduction and keyhole were correlated with the resulting melt pool depth. A distinct threshold between fusion modes was found by means of thermal emission and the powder processability of the metal powder. Consequently, this is dependent on the powder configuration within a powder layer and can thus be influenced by the nanoparticle formulation. Overall, it was found that nanoparticle dry-coating with low concentrated nanoparticles < 69 ppm is a viable tool for improving powder performance in metal powders for AM applications.

## CRediT authorship contribution statement

**Eric Gärtner:** Project administration, Conceptualization, Data curation, Investigation, Formal analysis, Methodology, Visualization, Writing – original draft, Writing – review & editing. **Arne Witte:** Data curation, Investigation, Writing – review & editing. **Nicolas J. Peter:** Data curation, Investigation, Writing – review & editing. **Vivek Devulapalli:** Data curation, Investigation, Writing – review & editing. **Nils Ellendt:** Writing – review & editing. **Gerhard Dehm:** Writing – review & editing. **Eric A. Jägle:** Writing – review & editing. **Volker Uhlenwinkel:** Funding acquisition, Supervision, Conceptualization, Writing – review & editing. **Lutz Mädler:** Funding acquisition, Resources, Supervision, Conceptualization, Writing – review & editing.

## Data availability

Data will be made available on request.

## Declaration of Competing Interest

The authors declare that they have no known competing financial interests or personal relationships that could have appeared to influence the work reported in this paper.

## Acknowledgement

We would like to thank the German research foundation for the financial support of the priority program SPP 2006 titled “Compositionally Complex Alloys – High Entropy Alloys (CCA-HEA)” (funding number UH 77/11-2, DE 796/13-2, JA 2482/3-2) and members of this priority program for fruitful interactions.

## Appendix A. Supplementary data

Supplementary data to this article can be found online at <https://doi.org/10.1016/j.matdes.2023.111626>.

## References

- [1] C. Meier, R. Weissbach, J. Weinberg, W.A. Wall, A. John Hart, Modeling and characterization of cohesion in fine metal powders with a focus on additive manufacturing process simulations 343 (2019) 855–866.
- [2] E. Gärtner, H.Y. Jung, N.J. Peter, G. Dehm, E.A. Jägle, V. Uhlenwinkel, L. Mädler, Reducing cohesion of metal powders for additive manufacturing by nanoparticle dry-coating, Powder Technol. 379 (2021) 585–595.
- [3] A.B. Yu, C.L. Feng, R.P. Zou, R.Y. Yang, On the relationship between porosity and interparticle forces, Powder Technol. 130 (2003) 70–76.
- [4] A. Castellanos, The relationship between attractive interparticle forces and bulk behaviour in dry and uncharged fine powders, Adv. Phys. 54 (2005) 263–376.
- [5] A.B. Spierings, M. Voegtkub, T. Bauer, K. Wegener, Powder flowability characterisation methodology for powder-bed-based metal additive manufacturing, Prog. Addit. Manuf. (2015).
- [6] R. Streubel, M.B. Wilms, C. Dofñate-Buendía, A. Weisheit, S. Barcikowski, J.H. Schleifenzbaum, B. Gökce, Depositing laser-generated nanoparticles on powders for additive manufacturing of oxide dispersed strengthened alloy parts via laser metal deposition, Japan. J. Appl. Phys., 57 (2018) 040310-040311-040310-040310.
- [7] X. Zhu, Q. Zhang, C. Huang, Y. Wang, C. Yang, F. Wei, Validation of surface coating with nanoparticles to improve the flowability of fine cohesive powders, Particuology 30 (2017) 53–61.
- [8] K. Meyer, Nanomaterialien als Fließregulierungsmittel, Universität Würzburg, Fakultät für Chemie und Pharmazie, Fakultät für Chemie und Pharmazie / Institut für Pharmazie und, Lebensmittelchemie (2003).
- [9] A. Phua, P.S. Cook, C.H.J. Davies, G.W. Delaney, Powder spreading over realistic laser melted surfaces in metal additive manufacturing, Addit. Manuf. Lett. 3 (2022) 100039.
- [10] E. Li, Z. Zhou, L. Wang, H. Shen, R. Zou, A. Yu, Particle scale modelling of melt pool dynamics and pore formation in selective laser melting additive manufacturing, Powder Technol. 397 (2022) 117012.
- [11] S. Wu, Z. Lei, M. Jiang, J. Liang, B. Li, Y. Chen, Experimental investigation and discrete element modeling for particle-scale powder spreading dynamics in powder-bed-fusion-based additive manufacturing, Powder Technol. 403 (2022) 117390.
- [12] W. Nan, M. Pasha, M. Ghadiri, Numerical simulation of particle flow and segregation during roller spreading process in additive manufacturing, Powder Technol. 364 (2020) 811–821.
- [13] Y. He, A. Hassanpour, A.E. Bayly, Linking particle properties to layer characteristics: Discrete element modelling of cohesive fine powder spreading in additive manufacturing, Addit. Manuf. 36 (2020) 101685.
- [14] H. Chen, Q. Wei, S. Wen, Z. Li, Y. Shi, Flow behavior of powder particles in layering process of selective laser melting: Numerical modeling and experimental verification based on discrete element method, Int. J. Mach. Tool Manu. 123 (2017) 146–159.
- [15] H. Chen, Q. Wei, Y. Zhang, F. Chen, Y. Shi, W. Yan, Powder-spreading mechanisms in powder-bed-based additive manufacturing: Experiments and computational modeling, Acta Mater. 179 (2019) 158–171.
- [16] Y. He, A. Hassanpour, A.E. Bayly, Combined effect of particle size and surface cohesiveness on powder spreadability for additive manufacturing, Powder Technol. 392 (2021) 191–203.
- [17] L. Wang, E.L. Li, H. Shen, R.P. Zou, A.B. Yu, Z.Y. Zhou, Adhesion effects on spreading of metal powders in selective laser melting, Powder Technol. 363 (2020) 602–610.
- [18] C. Meier, R. Weissbach, J. Weinberg, W.A. Wall, A.J. Hart, Critical influences of particle size and adhesion on the powder layer uniformity in metal additive manufacturing, J. Mater. Process. Technol. 266 (2019) 484–501.

- [19] L. Cao, Numerical simulation of the impact of laying powder on selective laser melting single-pass formation, *Int. J. Heat Mass Transf.* 141 (2019) 1036–1048.
- [20] K.Q. Le, C. Tang, C.H. Wong, A study on the influence of powder packing density on the melt track in the selective laser melting process, *Proceedings of the International Conference on Progress in Additive Manufacturing*, 2018, pp. 703–708.
- [21] M. Zheng, L. Wei, J. Chen, Q. Zhang, C. Zhong, X. Lin, W. Huang, A novel method for the molten pool and porosity formation modelling in selective laser melting, *Int. J. Heat Mass Transf.* 140 (2019) 1091–1105.
- [22] P. Wei, Z. Wei, Z. Chen, J. Du, Y. He, J. Li, Fundamentals of radiation heat transfer in AlSi10Mg powder bed during selective laser melting, *Rapid Prototyp. J.* 25 (2019) 1506–1515.
- [23] L. Haferkamp, L. Haudenschild, A. Spierings, K. Wegener, K. Riener, S. Ziegelmeier, G.J. Leichtfried, The Influence of Particle Shape, Powder Flowability, and Powder Layer Density on Part Density in Laser Powder Bed Fusion, *Metals* 11 (2021) 418.
- [24] K. Riener, N. Albrecht, S. Ziegelmeier, R. Ramakrishnan, L. Haferkamp, A.B. Spierings, G.J. Leichtfried, Influence of particle size distribution and morphology on the properties of the powder feedstock as well as of AlSi10Mg parts produced by laser powder bed fusion (LPBF), *Addit. Manuf.* 34 (2020) 101286.
- [25] M. Qu, Q. Guo, L.I. Escano, S.J. Clark, K. Fezzaa, L. Chen, Mitigating keyhole pore formation by nanoparticles during laser powder bed fusion additive manufacturing, *Addit. Manuf. Lett.* 3 (2022) 100068.
- [26] O. Pannitz, F. Großwendt, A. Lüdecke, A. Kwade, A. Röttger, J.T. Sehrt, Improved Process Efficiency in Laser-Based Powder Bed Fusion of Nanoparticle Coated Maraging Tool Steel Powder, *Materials* 14 (2021).
- [27] P. Mair, V.S. Goettgens, T. Rainer, N. Weinberger, I. Letofsky-Papst, S. Mitsche, G. Leichtfried, Laser powder bed fusion of nano-CaB<sub>6</sub> decorated 2024 aluminum alloy, *J. Alloy. Compd.* 863 (2021) 158714.
- [28] B. Li, B. Qian, Y. Xu, Z. Liu, F. Xuan, Fine-structured CoCrFeNiMn high-entropy alloy matrix composite with 12 wt% TiN particle reinforcements via selective laser melting assisted additive manufacturing, *Mater. Lett.* 252 (2019) 88–91.
- [29] D. Schwencik, N. Ellendt, J. Fischer-Bühner, P. Hofmann, V. Uhlenwinkel, A novel convergent-divergent annular nozzle design for close-coupled atomisation, *Powder Metall.* 60 (2017) 198–207.
- [30] D. Beckers, N. Ellendt, U. Fritsching, V. Uhlenwinkel, Impact of process flow conditions on particle morphology in metal powder production via gas atomization, *Adv. Powder Technol.* 31 (2020) 300–311.
- [31] K. Meyer, I. Zimmermann, Effect of glidants in binary powder mixtures, *Powder Technol.* 139 (2004) 40–54.
- [32] K. Taherkhani, E. Sheydaeiyan, C. Eischer, M. Otto, E. Toyserkani, Development of a defect-detection platform using photodiode signals collected from the melt pool of laser powder-bed fusion, *Addit. Manuf.* 46 (2021) 102152.
- [33] A. Gaikwad, B. Giera, G.M. Guss, J.-B. Forien, M.J. Matthews, P. Rao, Heterogeneous sensing and scientific machine learning for quality assurance in laser powder bed fusion – A single-track study, *Addit. Manuf.* 36 (2020) 101659.
- [34] J.-B. Forien, N.P. Calta, P.J. DePond, G.M. Guss, T.T. Roehling, M.J. Matthews, Detecting keyhole pore defects and monitoring process signatures during laser powder bed fusion: A correlation between in situ pyrometry and ex situ X-ray radiography, *Addit. Manuf.* 35 (2020) 101336.
- [35] W.E. King, H.D. Barth, V.M. Castillo, G.F. Gallegos, J.W. Gibbs, D.E. Hahn, C. Kamath, A.M. Rubenchik, Observation of keyhole-mode laser melting in laser powder-bed fusion additive manufacturing, *J. Mater. Process. Technol.* 214 (2014) 2915–2925.
- [36] J.-B. Forien, G.M. Guss, S.A. Khairallah, W.L. Smith, P.J. DePond, M.J. Matthews, N.P. Calta, Detecting missing struts in metallic micro-lattices using high speed melt pool thermal monitoring, *Addit. Manuf. Lett.* 4 (2023) 100112.
- [37] J. Laube, S. Salameh, M. Kappl, L. Mädler, L. Colombo Ciacci, Contact Forces between TiO<sub>2</sub> Nanoparticles Governed by an Interplay of Adsorbed Water Layers and Roughness, *Langmuir* 31 (2015) 11288–11295.
- [38] V. Baric, J. Laube, S. Salameh, L. Colombo Ciacci, L. Mädler, A Contact Model for the Discrete Element Simulations of Aggregated Nanoparticle Films, in: S. Antonyuk (Ed.), *Particles in Contact: Micro Mechanics*, Springer International Publishing, Cham, Micro Process Dynamics and Particle Collective, 2019, pp. 339–358.
- [39] R.L. Carr, Evaluating flow properties of solids, *Chem. Eng.* 72 (1965) 163–168.
- [40] R.E. Riley, H.H. Hausner, Effect of particle size distribution on the friction in a powder mass, *Int. J. Powder Met.* 6 (1970) 6.
- [41] M.Y. Shaheen, A.R. Thornton, S. Luding, T. Weinhart, The influence of material and process parameters on powder spreading in additive manufacturing, *Powder Technol.* 383 (2021) 564–583.
- [42] H. Chen, T. Cheng, Z. Li, Q. Wei, W. Yan, Is high-speed powder spreading really unfavourable for the part quality of laser powder bed fusion additive manufacturing?, *Acta Mater.* 231 (2022) 117901.
- [43] T.-C. Lin, C. Cao, M. Sokoluk, L. Jiang, X. Wang, J.M. Schoenung, E.J. Lavernia, X. Li, Aluminum with dispersed nanoparticles by laser additive manufacturing, *Nat. Commun.* 10 (2019) 4124.
- [44] C. Schwerz, L. Nyborg, Linking In Situ Melt Pool Monitoring to Melt Pool Size Distributions and Internal Flaws in Laser Powder Bed Fusion, *Metals* 11 (2021).
- [45] J.-N. Zhu, E. Borisov, X. Liang, E. Farber, M.J.M. Hermans, V.A. Popovich, Predictive analytical modelling and experimental validation of processing maps in additive manufacturing of nitinol alloys, *Addit. Manuf.* 38 (2021) 101802.
- [46] J. Yang, J. Han, H. Yu, J. Yin, M. Gao, Z. Wang, X. Zeng, Role of molten pool mode on formability, microstructure and mechanical properties of selective laser melted Ti-6Al-4V alloy, *Mater. Des.* 110 (2016) 558–570.
- [47] R. Cunningham, C. Zhao, N. Parab, C. Kantzos, J. Pauza, K. Fezzaa, T. Sun, A.D. Rollett, Keyhole threshold and morphology in laser melting revealed by ultrahigh-speed x-ray imaging, *Science* 363 (2019) 849–852.
- [48] C. Zhao, N.D. Parab, X. Li, K. Fezzaa, W. Tan, A.D. Rollett, T. Sun, Critical instability at moving keyhole tip generates porosity in laser melting, *Science* 370 (2020) 1080–1086.
- [49] M. Tang, P.C. Pistorius, J.L. Beuth, Prediction of lack-of-fusion porosity for powder bed fusion, *Addit. Manuf.* 14 (2017) 39–48.
- [50] S.K. Rauniyar, K. Chou, Melt Pool Analysis and Mesoscale Simulation of Laser Powder Bed Fusion Process (L-PBF) with Ti-6Al-4V Powder Particles, *JOM* 71 (2019) 938–945.
- [51] D.B. Hann, J. Iammi, J. Folkes, A simple methodology for predicting laser-weld properties from material and laser parameters, *J. Phys. D Appl. Phys.* 44 (2011) 445401.
- [52] Y. Chen, S.J. Clark, C.L.A. Leung, L. Sinclair, S. Marussi, M.P. Olbinado, E. Boller, A. Rack, I. Todd, P.D. Lee, In-situ Synchrotron imaging of keyhole mode multi-layer laser powder bed fusion additive manufacturing, *Appl. Mater. Today* 20 (2020) 100650.